JGP Journal of General Physiology

ARTICLE

The basic residues in the Orai1 channel inner pore promote opening of the outer hydrophobic gate

Megumi Yamashita[1]*, Christopher E. Ing[2,3]*, Priscilla See-Wai Yeung[1], Mohammad M. Maneshi[1], Régis Pomès[2,3], and Murali Prakriya[1]

Store-operated Orai1 channels regulate a wide range of cellular functions from gene expression to cell proliferation. Previous studies have shown that gating of Orai1 channels is regulated by the outer pore residues V102 and F99, which together function as a hydrophobic gate to block ion conduction in resting channels. Opening of this gate occurs through a conformational change that moves F99 away from the permeation pathway, leading to pore hydration and ion conduction. In addition to this outer hydrophobic gate, several studies have postulated the presence of an inner gate formed by the basic residues R91, K87, and R83 in the inner pore. These positively charged residues were suggested to block ion conduction in closed channels via mechanisms involving either electrostatic repulsion or steric occlusion by a bound anion plug. However, in contrast to this model, here we find that neutralization of the basic residues dose-dependently abolishes both STIM1-mediated and STIM1-independent activation of Orai1 channels. Molecular dynamics simulations show that loss of the basic residues dehydrates the pore around the hydrophobic gate and stabilizes the pore in a closed configuration. Likewise, the severe combined immunodeficiency mutation, Orai1 R91W, closes the channel by dewetting the hydrophobic stretch of the pore and stabilizing F99 in a pore-facing configuration. Loss of STIM1-gating in R91W and in the other basic residue mutants is rescued by a V102A mutation, which restores pore hydration at the hydrophobic gate to repermit ion conduction. These results indicate that the inner pore basic residues facilitate opening of the principal outer hydrophobic gate through a long-range effect involving hydration of the outer pore.

Introduction

In many animal cells, Ca^{2+} release-activated Ca^{2+} (CRAC) channels function as a major route of Ca^{2+} entry to mobilize cellular Ca^{2+} elevations following stimulation of G-protein–coupled or tyrosine kinase receptors. Endowed with several distinguishing biophysical features including exquisite Ca^{2+} selectivity and a low unitary conductance (Prakriya and Lewis, 2015), canonical CRAC channels are assembled from two proteins: Orai1, the pore-forming subunit, and STIM1, the endoplasmic reticulum Ca^{2+} sensor and CRAC channel activator (Prakriya and Lewis, 2015). STIM1 senses changes in the ER luminal Ca^{2+} concentration, and in response to depletion of ER stores, accumulates at the ER–plasma membrane junctions, where it binds to and gates Orai1 channels. The ensuing Ca^{2+} entry mediates many critical effector functions, including gene transcription, motility, and cell proliferation (Prakriya and Lewis, 2015). Genetic studies have shown that patients with loss-of-function (LOF) or gain-of-function (GOF) mutations in STIM1 or Orai1 suffer from life-threatening immunodeficiencies, autoimmunity, coagulation defects, and muscle weakness (Feske, 2009, 2010; Lacruz and Feske, 2015; Prakriya and Lewis, 2015), underscoring the importance of CRAC channels for human health. As a result, CRAC channels have emerged as potential targets for the treatment of chronic inflammation, autoimmunity, and related diseases.

Since the discovery of the Orai proteins as pore-forming subunits of CRAC channels in 2006, a great deal of effort has been directed toward understanding the pore opening mechanism. The crystallographic structure of *Drosophila melanogaster* Orai (dOrai) solved several years ago indicates the channel is a hexamer (Hou et al., 2012). The transmembrane domains (TMs) of each Orai1 subunit are arranged in concentric rings around a centrally located pore formed by six TM1 helices, and TMs 2 and 3 forming a tightly interlocked ring between TM1 and the outermost TM4 helices. Recent studies using state-dependent accessibility analysis of F99 and molecular dynamics simulations have found that pore opening is triggered by the release of a hydrophobic gate formed by two rings of pore-lining hydrophobic residues, F99 and V102. These residues block the passage of ions in the pore by favoring the dry or dewetted state of the

[1]Department of Pharmacology, Northwestern University, Feinberg School of Medicine, Chicago, IL; [2]Molecular Medicine, Hospital for Sick Children, Toronto, Canada; [3]Department of Biochemistry, University of Toronto, Toronto, Canada.

*M. Yamashita and C.E. Ing contributed equally to this paper; Correspondence to Murali Prakriya: m-prakriya@northwestern.edu; Régis Pomès: pomes@sickkids.ca.

https://doi.org/10.1085/jgp.201912397

gate. Opening of this gate is mediated by small (~20°) rotation (or twisting) and concomitant dilation of the pore helices resulting in movement of the bulky F99 side chains away from the pore lumen (Yamashita et al., 2017; Yeung et al., 2018; Bulla et al., 2019; Dong et al., 2019). This model is supported by several observations: (1) mutations that lower the hydrophobicity of V102 or F99 lead to constitutively permeant channels and increased pore hydration (McNally et al., 2012; Dong et al., 2013; Yamashita et al., 2017), (2) accessibility of a cysteine residue introduced at F99 to pore-applied thiol reagents (Cd^{2+}) is seen only in STIM1-free but not STIM1-bound channels (Yamashita et al., 2017), and (3), MD simulations of constitutively active Orai1 variants at the H134 locus show discrete pore helix rotations (~15–20°) accompanied by a small amount of pore dilation (~2 Å in diameter) at F99 (Yeung et al., 2018; Bulla et al., 2019). Because these conformational changes at the hydrophobic gate would also be expected to change the arrangement of E106 residues forming the nearby Ca^{2+} selectivity filter, this gating mechanism also explains the covariation of ion selectivity and STIM1-mediated channel gating in CRAC channels (McNally et al., 2012; Yen and Lewis, 2018).

Yet, the story is not so simple. In addition to the outer hydrophobic gate described above, several reports have suggested that the CRAC channel pore also harbors a putative second gate, located at the cytoplasmic end of the pore (Zhang et al., 2011; Hou et al., 2012; Frischauf et al., 2017). This idea has its roots in a peculiar feature of the CRAC channel, three rings of positively charged residues formed by R91, K87, and R83 located in the TM1 extension helix, which collectively present a cluster of 18 positive charges in the inner pore. The presence of positive charges in the pore is an unusual feature for cationic channels and has fueled speculations that these charges repel Ca^{2+} ions to impede ion flow in the closed state, in effect functioning as an inner channel gate (Zhang et al., 2011; Hou et al., 2012). However, the mechanism through which these residues regulate gating remains unclear. One study has suggested that the basic residues could regulate gating via pore blockade mediated by a bound anion plug, which is released via dilation of the inner pore helices during channel opening (Hou et al., 2012). A second study suggests that the R91 gate opens during channel activation by twisting of its side chain through a hydrogen bond interaction with S90 of the neighboring subunit (Frischauf et al., 2017). Yet another study has postulated that the hub of positive charges promotes cation permeation via an anion-assisted mechanism (Dong et al., 2014). Finally, two recent structural studies have found that the inner pore of the constitutively active H206A and P288L mutant channels (corresponding to H134A and P245L in hOrai1) is considerably wider than that of the closed dOrai crystal structure, leading them to conclude that inner pore widening is a key conformational change associated with pore opening (Hou et al., 2018; Liu et al., 2019). However, given the low resolution (<5 Å) of these structures, especially in the pore helices, it was impossible to draw conclusions regarding the orientation or conformation of pore-lining side chains from these studies. Thus, the exact mechanism by which the basic charges regulate pore opening and ion conduction remains elusive.

In this study, we address the role of the inner pore basic residues in Orai1 channel gating using a combination of experimental and computational approaches. Our results suggest that the inner pore basic residues do not function as a channel gate controlling ion movement in the CRAC channel pore. Instead, the basic residues appear to be required for an entirely different role, tuning the level of pore hydration at the hydrophobic gate to permit opening and closing of the channel. This long-range effect of the basic residues promotes pore opening and represents a novel mode of regulating ion channel gating.

Materials and methods

Cells

HEK293 cells were maintained in suspension at 37°C with 5% CO_2 in CD293 medium supplemented with 4 mM GlutaMAX (Gibco). For imaging and electrophysiology, cells were plated onto poly-L-lysine–coated coverslips 1 d before transfection and grown in a medium containing 44% Dulbecco's Modified Eagle Medium (Corning), 44% Ham's F12 (Corning), 10% fetal bovine serum (HyClone), 2 mM glutamine (Gln), 50 U/ml penicillin, and 50 µg/ml streptomycin.

Plasmids and transfections

The Orai1 mutants employed for electrophysiology were engineered into either the previously described pEYFP-N1 vector (Clontech) to produce C-terminally tagged Orai1-YFP proteins. mCherry-STIM1 was a kind gift of R. Lewis (Stanford University, Stanford, CA). All mutants were generated by the QuikChange Mutagenesis kit (Agilent Technologies), and the mutations were confirmed by DNA sequencing. For electrophysiology, the indicated Orai1 constructs were transfected into HEK293 cells either alone (200 ng DNA per coverslip) or together with STIM1 (100 ng Orai1 and 500 ng STIM1 DNA per coverslip). For confocal microscopy, cells were transfected with Orai1-YFP (200 ng DNA per coverslip). All transfections were performed using Lipofectamine 2000 (Thermo Fisher Scientific) 24–48 h before electrophysiology or imaging experiments.

Solutions and chemicals

The standard extracellular Ringer's solution used for electrophysiological experiments contained 130 mM NaCl, 4.5 mM KCl, 20 mM $CaCl_2$, 10 mM tetraethylammonium chloride, 10 mM D-glucose, and 5 mM HEPES, pH 7.4 with NaOH. For the confocal imaging studies, the Ringer's solution contained 2 mM $CaCl_2$ and 150 mM NaCl with the other components as above. The divalent-free solution Ringer's solution contained 150 mM NaCl, 10 mM HEDTA, 1 mM EDTA, 10 mM tetraethylammonium chloride, and 5 mM HEPES, pH 7.4. The internal pipette solution contained 135 mM Cs aspartate, 8 mM $MgCl_2$, 8 mM Cs-BAPTA, and 10 mM HEPES, pH 7.2 with CsOH. Stock solutions of Bis(2-mercaptoethylsulfone) and diamide were prepared by dissolving reagents in water and DMSO, respectively, and stored at −20°C. For final administration, these reagents were prepared immediately before use during the patch-clamp experiment by thawing the stock solutions and resuspending the reagents in ice-cold extracellular solutions.

Solutions and drugs were applied using a multibarrel perfusion pipette.

Electrophysiology

Currents were recorded in the standard whole-cell configuration at room temperature on an Axopatch 200B amplifier (Molecular Devices) interfaced to an ITC-18 input/output board (Instrutech). Single polygonal-shaped cells were chosen for patching. Routines developed by R. S. Lewis (Stanford University) on the Igor Pro software (Wavemetrics) were employed for stimulation, data acquisition, and analysis. Data are corrected for the liquid junction potential of the pipette solution relative to Ringer's in the bath (10 mV). The holding potential was +30 mV. The standard voltage stimulus consisted of a 100-ms step to −100 mV followed by a 100-ms ramp from −100 to +100 mV applied at 1-s intervals. CRAC current (I_{CRAC}) was typically activated by passive depletion of ER Ca^{2+} stores by intracellular dialysis of 8 mM BAPTA. All currents were acquired at 5 kHz and low-pass filtered with a 1 kHz Bessel filter built into the amplifier. All data were corrected for leak currents collected in 100–200 µM $LaCl_3$.

Data analysis of electrophysiology results

Analysis of current amplitudes was performed by measuring the peak currents during the 100-ms pulse to −100 mV. For the bar graphs shown in the paper, current amplitudes were determined by averaging the maximal current densities in each cell following passive activation of CRAC currents in response to intracellular dialysis of BAPTA (maximal current is reached typically 300–400 s following whole-cell break-in). Fractional blockade of CRAC current by Cd^{2+} was quantified as blockade = $(1 - I_b / I_{Ctrl})$, where I_b is the Orai1 current in the presence of Cd^{2+}, and I_{Ctrl} is the Orai1 current before application of the blocker. Statistical comparisons were performed using unpaired *t* tests as indicated.

Confocal microscopy

HEK293 cells expressing various Orai1-YFP mutants were imaged on an Andor XDI Revolution spinning-disk confocal microscope equipped with a 100× oil immersion objective. Fluorophores were excited with 515 nm (YFP) laser diodes with the intensity of laser light attenuated to 20–40%. Images were obtained at 512 × 512 pixels at an exposure of 200–500 ms per frame and a slice thickness of 0.8 µm. Images analysis was performed using ImageJ software (National Institutes of Health).

MD simulations

Molecular models were constructed based on the crystal structure of the dOrai channel (PDB accession no. 4HKR; Hou et al., 2012) using methods previously described (Yeung et al., 2018). Briefly, system preparation was performed using the CHARMM-GUI membrane builder (Jo et al., 2007). Missing residues of the M1-M2 loop (amino acids 181–190) and the M2-M3 loop (amino acids 220–235) were modeled de novo using MODELLER (Fiser and Sali, 2003). The C terminus was truncated at residue 329 for all chains, and the N and C termini were acetylated and amidated, respectively. The protein was embedded within a hydrated 1-palmitoyl,2-oleoyl-sn-glycero-3-phosphocholine bilayer with 150 mM NaCl to obtain a hexagonal cell with box dimensions 10.42 × 10.42 × 12.65 nm^3. Pore water molecules were not modeled. The simulation cell consisted of ∼112,000 atoms. Single point mutations were made using CHARMM-GUI to create the V174A, 3S (R155S/K159S/R163S, R155S/K159S/R163S/V174A, R155S/K159S/R163S/W148A), 2S (K159S/K163S, K159S/K163S/V174A), K163W, and K163W/V174A systems. The CHARMM36 force field was used for proteins (MacKerell et al., 1998; Best et al., 2012), ions, and lipids (Klauda et al., 2010) along with the TIP3P water model (Jorgensen et al., 1983).

All simulations were performed using GROMACS 2016.3 (Abraham, 2015) without modification of the CHARMM-GUI output parameters (with the exception of additional equilibration steps and extended production simulation length). Lennard–Jones interactions were cut off at 1.2 nm, and a force-based switching function with a range of 1.0 nm was used. Electrostatic interactions were calculated using particle-mesh Ewald (Darden et al., 1993; Essmann et al., 1995) with a real-space cut-off distance of 1.2 nm. Nonbonded interactions were calculated using Verlet neighbor lists (Verlet, 1967; Pall and Hess, 2013). All simulations were performed at constant temperature (323.15 K) and pressure (1 atm) using the Nosé–Hoover thermostat (Nose, 1984; Hoover, 1985) with temperature coupling of 1.0 ps and the Parrinello–Rahman barostat (Parrinello and Rahman, 1980; Nose and Klein, 1983) with a time constant of 5.0 ps, respectively. All hydrogen bonds were constrained using the LINCS algorithm (Hess, 2008). The integration time step was 2 fs. All systems followed the standard energy minimization and six-step equilibration procedure of CHARMM-GUI (Jo et al., 2007), followed by two successive 10-ns protein-restrained simulations conducted in the NPT ensemble. In these equilibration steps, quadratic position restraints were applied first to all main-chain backbone atoms and then Cα atoms, with a force constant of 1,000 kJ mol^{-1} nm^{-2}. 20 simulation repeats were created for WT, V174A, 3S, and 3S/V174A systems, 10 simulation repeats were created for the 3S/W148A, K163W, and K163W/V174A systems, and 30 simulation repeats were created for both 2S systems, where all repeats had randomized initial velocities for production simulations. Production simulations were conducted for 400–500 ns for all simulation repeats for an aggregate total of 83.457 µs.

Prior to analysis, all simulation frames were rotated such that the principal axis formed by TM1 helix Cα atoms was aligned to the box vector z. Analysis was performed on all simulation frames at 1.0-ns intervals after removing the first 100 ns of data from each simulation repeat, with the exception of HOLE analysis (Smart et al., 1996), which was performed on all simulation frames at 20.0-ns intervals after removing the first 100 ns of data. All axial coordinates were measured with respect to the center of mass of the pore helix Cα atoms (residues 141–174). Axial histograms of water oxygen atoms, Na^+ and Cl^-, were computed within a 1-nm-radius cylinder centered at the pore center of mass. The average radius of the pore at position F171 was measured by computing the distance between the center of mass of the pore in the x–y plane and the average position of C-α atoms of residues 167–175 for each subunit and averaging over all

subunits. The number of water molecules in the hydrophobic stretch was computed using the z-axis boundaries defined by Yeung et al. (10–25 Å; Yeung et al., 2018). Error bars were computed using SEM over all simulation repeats. In the results section, the mean average F171 Cα rotation was reported with respect to the crystallographic orientation of the F171 side-chain in our coordinate system (30.636°, PDB accession no. 4HKR). Statistical analysis was performed to test the hypothesis that the distribution of mean radial angles in the WT dataset and alternative mutants have the same mean value. For our significance test, the average radial angle at position F171 was extracted from each of the six subunits for all simulation repeats after 100 ns of equilibration was removed from the start of each trajectory. These values were compared with the same set of values in the WT system for all mutant systems, resulting in (238, 238, 238, 298, 298, 178, 178, and 178) degrees of freedom for our statistical test for each system (V174A, 3S, 3S/V174A, 3S/W148A, 2S, 2S/V174A, K163W, and K163W/V174A), respectively. The P values from a two-sided Welch's *t* test for each system (2.0×10^{-16}, 2.5×10^{-2}, 2.2×10^{-3}, 2.1×10^{-1}, 1.5×10^{-10}, 7.9×10^{-1}, 4.7×10^{-2}, 1.7×10^{-2}, 1.0×10^{-3}) indicate that the differences between the mean of these distributions with respect to WT simulations are significant ($P < 0.05$), with two exceptions. The 3S/W148A mutant may require additional simulation repeats, and the 2S/V174A mutation is a system where we expect that V174A may restore pore helix rotation back to the levels observed in WT simulations.

Online supplemental material

Fig. S1 shows functional analysis of inner pore cysteine mutants including current amplitudes and blockade by Cd^{2+}. Fig. S2 shows loss of function phenotypes of the inner pore Ala and Ser mutants. Fig. S3 shows functional characterization of the W76S and W76A mutants in the 3S background and molecular dynamics simulations showing that the addition of W76A (W148A in dOrai) does not rescue dehydration of the hydrophobic gate caused by the 3S mutation.

Results

Previous studies have suggested that the cationic residues (Fig. 1 A) facing the ion permeation pathway, and R91 in particular, control Orai1 gating by repelling Ca^{2+} ions or binding Cl^- ions to create an anion plug that blocks conduction in closed channels (Zhang et al., 2011; Hou et al., 2012; Frischauf et al., 2017). Channel activation was suggested to occur due to displacement of R91 away from the pore axis, which presumably would lower an electrostatic energy barrier presented by this residue, or via dilation of the inner pore, leading to release of the anion plug (Zhang et al., 2011; Hou et al., 2012; Frischauf et al., 2017). These gating models make specific predictions regarding the consequences of charge neutralization mutations on closed channel stability and channel opening, which we tested as described below.

Mutations of the basic residues do not destabilize the closed channel state

First, we assessed the consequences of destroying the potential R91 gate for channel function. If R91 functions as an electrostatic barrier to impede cation flow in closed channels (Zhang et al., 2011; Frischauf et al., 2017), one would expect that mutations lowering the electrostatic barrier at R91 may destabilize the closed channel state to promote pore opening. Such an effect may be analogous to constitutive channel activation elicited by mutations in the V102-F99 hydrophobic gate, which lower the free energy for hydration to yield constitutively permeant Orai1 channels (McNally et al., 2012; Dong et al., 2013; Yamashita et al., 2017). However, mutations of R91 to various uncharged polar residues did not evoke constitutive channel activation (Fig. 1 B). For example, R91A remained closed in the absence of STIM1, but could be gated by coexpressing STIM1. Even substitutions to negatively charged residues (R91D/E) failed to yield constitutive Orai1 currents, and yet, these mutants could be readily opened by STIM1 and exhibited functional properties including current amplitudes, current–voltage (I–V) relationships, and reversal potentials (V_{rev}) comparable to WT Orai1 channels gated by STIM1 (Fig. 1, B and C). Similarly, R83C and K87C were closed in the absence of STIM1 but could be readily activated by STIM1 (Fig. S1, A–C). As previously shown by Derler et al. (2009), nonpolar amino acids at R91 caused loss of gating (Fig. 1 C), indicating a strict requirement for the presence of polar amino acids at this locus for channel activation. Together, these results indicate that removal of the putative electrostatic inner gate at R91, K87, and R83 does not evoke constitutive ion conduction in resting Orai1 channels, nor does it prevent STIM1-mediated channel activation.

An argument in favor of the idea that R91 functions as an inner gate has come from observations showing that the human mutation, R91W, produces nonconducting Orai1 channels due to the formation of a hydrophobic plug at the base of TM1 (Zhang et al., 2011). Steric occlusion of ion flux by Trp at this locus has been used to support the idea that the native R91 side-chains could similarly occlude ion conduction in unliganded WT Orai1 channels (Zhang et al., 2011; Hou et al., 2012). However, as shown (Fig. 1 D), introduction of Trp at the other pore-lining positions, V102, G98, and L95, also ablated Orai1 channel activity in the presence of STIM1. Thus, the effect of the Trp mutation at R91 in abrogating channel function is not unique to R91 but occurs at all pore-lining positions, likely due to the narrow Orai1 pore dimensions along the length of TM1.

Disrupting a putative interaction between R91 and S90 does not interfere with Orai1 gating

From the analysis of side-chain fluctuations using MD simulations, a recent study concluded that in the constitutively active Orai1 mutant H134A, R91 side-chains interact with nearby S90 residues from the neighboring subunits (Frischauf et al., 2017). This interaction was postulated to displace R91 away from the pore and drive pore opening (Frischauf et al., 2017). A simple prediction from this model is that mutations at S90 that interrupt this interaction should inhibit STIM1-mediated channel gating. We tested this prediction using amino acid substitutions at S90 (S90A and S90G) that preclude hydrogen bond interactions with R91. In the presence of STIM1, neither mutation abolished Orai1 gating, with both variants yielding STIM1-gated currents with amplitudes >10 pA/pF (Fig. 1 E). This result is

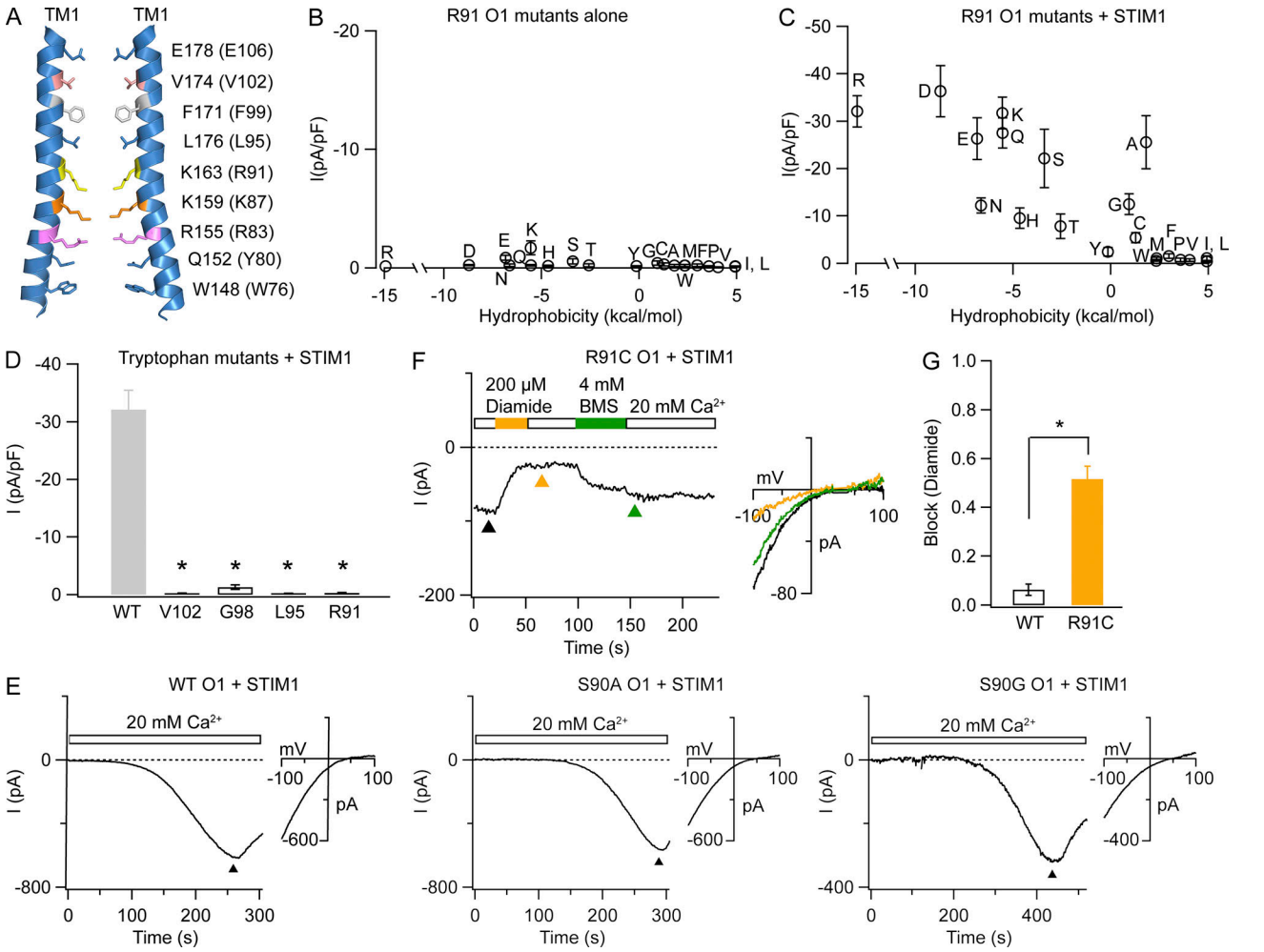

Figure 1. **R91 is unlikely to function as an Orai1 channel gate. (A)** A side view of the dOrai crystal structure (PDB accession no. 4HKR) showing two pore helices and the key pore residues. Amino acid numbers corresponding to human Orai1 are shown in parentheses. **(B and C)** Analysis of R91X mutants. The graphs show current densities of R91X mutants in the absence and presence of STIM1 plotted against hydrophobicity of the introduced amino acid. Each point represents the mean of 6–9 cells. **(D)** Introduction of a Trp residue at any pore-lining position blocks channel activity. Current densities of the indicated Trp pore mutants were measured in the presence of STIM1. **(E)** S90A and S90G Orai1 channels exhibit store-operated gating by STIM1, similar to WT Orai1 channels. Reversal potentials are >65 mV (WT; n = 9), 62 ± 5 mV (S90A; n = 6), and 50 ± 3 mV (S90G; n = 6). The inset shows current-voltage relationships (I–Vs) obtained at the time point indicated by the arrowhead. **(F)** The oxidizing agent, diamide (200 µM), inhibits currents in R91C Orai1 channels, which are readily reversed by the reducing agent, Bis(2-mercaptoethylsulfone; BMS). I-V relationships obtained at the time points indicated by the arrowheads are shown in the inset. **(G)** Summary of diamide inhibition in WT and R91C channels. Values are mean ± SEM (*, P < 0.05, Student's t test).

consistent with a previous study showing that the R91A and the S89G/S90G mutants are also effectively activated by STIM1 (Derler et al., 2009), which suggests that rotation or twisting of R91 side chains is not essential for Orai1 activation. Indeed, cysteine accessibility analysis of the R91C mutant indicates that the thiol-reactive reagent, Cd^{2+}, can readily block STIM1-activated R91C Orai1 channels (Fig. S1, D–F; McNally et al., 2009). Similarly, as previously demonstrated (Zhang et al., 2011), the oxidizing agent diamide rapidly induced channel blockade in R91C Orai1 channels (Fig. 1, F and G) due to the formation of an intersubunit disulfide bond across the pore. These results indicate that R91C side-chains are readily accessible to pore-applied thiol reagents in the open channel state. Our MD simulations of WT, V174A (hOrai1 V102A), and the GOF H206S (hOrai1 H134S) channels corroborated these experimental results: specifically, the interchain/neighboring chain interactions between K163 (hOrai1 R91) side-chain hydrogen bonds to S162 (hOrai1 S90) were observed in only 0.35 ± 0.21% of frames in WT and 0.49 ± 0.18% of frames in the V174A mutant. Retrospective analysis of previously reported H206S simulations (Yeung et al., 2018) further revealed occurrences of K163-S162 interactions in only ∼1% of frames (0.99 ± 0.39%). Taken together, these results indicate that R91C side chains remain pore-facing in the open state and are unlikely to twist away from the pore during pore opening. Considered as a whole, these results suggest that R91 does not stabilize the closed channel state.

Progressively neutralizing the inner pore basic residues results in charge-dependent loss of channel gating

If R91 and the other basic residues do not directly contribute to stabilizing the closed channel state, what are their roles in ion conduction? To begin to address this question, we progressively

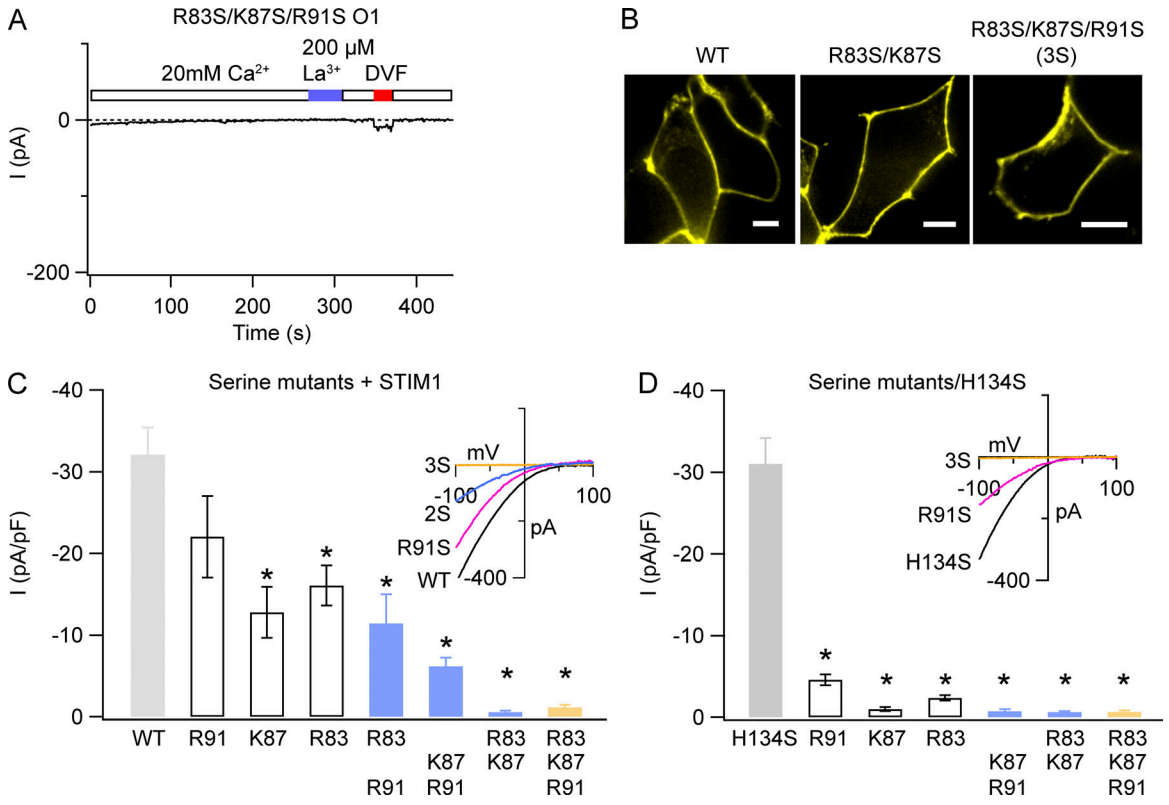

Figure 2. **Neutralizing the inner pore basic residues results in charge-dependent loss of Orai1 gating. (A)** The 3S mutant (R83S/K87S/R91S) is not constitutively active in the absence of STIM1. The trace shows a representative example from cell expressing R83S/K87S/R91S Orai1-YFP. DVF, divalent-free solution. **(B)** Confocal images of WT, R83S/K87S, and R83S/K87S/R91S (3S) mutants. In all cases, the Orai1 variants were tagged at the C terminus with YFP. Scale bar, 5 µm. **(C)** Summary of current densities of WT or the indicated Ser Orai1 mutants coexpressed with mCherry STIM1 (n = 6–9 cells per condition). **(D)** Summary of the current densities of the indicated Orai1 Ser mutants in the GOF H134S background (expressed without STIM1). Insets show I–V relationships. Values are mean ± SEM (n = 6–8 per condition; *, significantly different than WT; P < 0.05, Student's t test).

neutralized the three basic residues by replacing them either individually or in combinations with Ser, Ala, or Gln.

Removal of the positive charges individually, pairwise, or as a group (R83S/K87S/R91S [3S] or R83A/K87A/R91A [3A]) did not produce any level of constitutive Orai1 current in the absence of STIM1 (Fig. 2 A; I = −0.16 ± 0.05 pA/pF for the 3S mutant; I = −0.21 ± 0.07 pA/pF for the 3A mutant, where I is current amplitude), consistent with recent observations (Hou et al., 2018) indicating that the removal of some or even all of the basic charges does not destabilize the closed channel state. More surprisingly, neutralization of the basic residues resulted in loss of Orai1 channel activation when STIM1 was coexpressed, with the removal of all inner pore basic charges (3S or 3A) completely abrogating STIM1-mediated Orai1 currents (Fig. 2 C; and Fig. S2 A; see also Hou et al., 2018), indicating that the mutations destabilize the open channel state. The loss of current was not due to impaired protein expression as assessed by Orai1-YFP plasma membrane fluorescence (Fig. 2 B), signifying that the channels are indeed correctly targeted to the plasma membrane. Interestingly, loss of gating exhibited a curious charge dependence with removal of just two of the three native amino acids (R83S/K87S or K87S/R91S(2S)) producing significantly smaller currents than currents in single R91S, K87S, or R83S substitutions, which in turn were smaller than WT channels (Fig. 2 C). A Y80S/R83S/K87S triple mutant was also nonfunctional and failed to exhibit activity when coexpressed with STIM1 (Fig. S2 B). Thus, these results indicate that removal of the inner pore basic residues abrogates normal STIM1-mediated Orai1 gating.

It has been recently shown that several mutations at H134 evoke constitutively active Orai1 channels with permeation properties resembling STIM1-gated channels (Frischauf et al., 2017; Yeung et al., 2018). In particular, the H134S variant evokes robust Orai1 channel activation through the release of a steric brake at the TM1-TM2/3 ring interface (Yeung et al., 2018) to open the gate and provides a useful tool to examine Orai1 gating in the absence of STIM1. Do the basic residues also affect H134S-mediated constitutive activation? We tested this by introducing the H134S mutation in the single, double, and triple inner pore basic residue mutants. Neutralizing the inner pore basic residues resulted in the loss of channel activity in the constitutively active H134S mutant channel with a charge dependence resembling of the loss of gating seen in STIM1-gated channels (Fig. 2 D). In fact, in the H134S background, removal of just one of the three basic residues was sufficient to decrease the H134S currents by >80%, and removing two of the three basic residues abolished most of the H134S current. This result demonstrates that gating of the constitutively active H134S Orai1 channels is even more sensitive to the loss of the inner pore

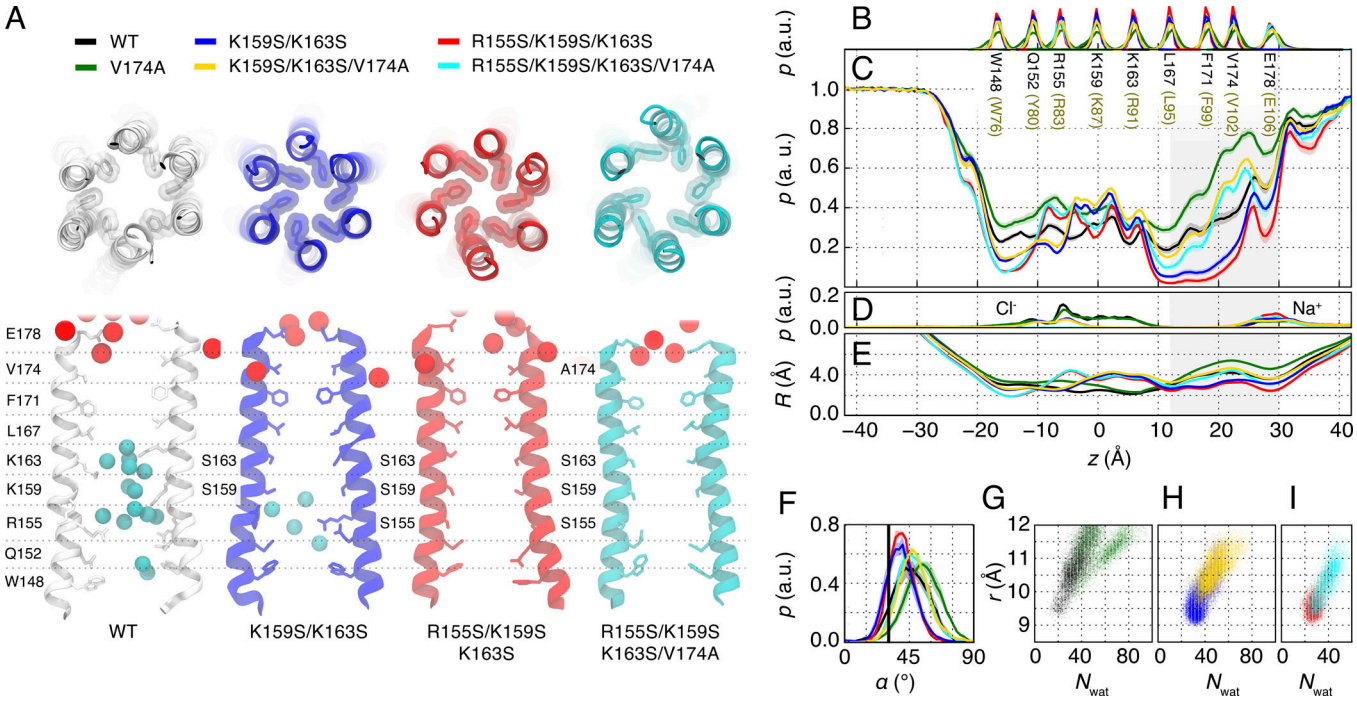

Figure 3. **Molecular dynamics simulations indicate that interactions in the basic region are correlated with pore hydration of the hydrophobic gate and the conformation of the F99 residue. (A)** Top: Molecular renderings of snapshots from MD simulations of WT (gray), K159S/K163S (blue), R155S/K159S/K163S (red), and R155S/K159S/K163S/V174A (aqua) as viewed from the top. Bottom: Pairs of diagonal subunits viewed from the side. Na^+ and Cl^- are depicted as red and cyan spheres, respectively. **(B)** Probability distributions of protein Cα atoms for pore-lining residues along the pore axis (z), averaged over all subunits for all simulation repeats. The residue numbering corresponding to human Orai1 are shown in brown. Data in A–I were computed from simulations of WT (black), V174A (green), K159S/K163S (blue), K159S/K163S/V174A (yellow), R155S/K159S/K163S (red), and R155S/K159S/K163S/V174A (aqua) mutant channels. **(C and D)** Relative probability distribution of water oxygen atoms (C), Na^+, and Cl^- ions (D) along the pore axis (z), normalized with respect to bulk water. All probability distributions are quantified with arbitrary units (a.u.). **(E)** Average pore radius computed using HOLE (*R*). **(F)** Probability distribution of the radial angle of residue 171 (α), defined as the angle between the pore axis, the center of mass of the two helical turns centered at residue 171, and the Cα atom of residue 171. The mean and standard error of mean of these distributions across all simulation repeats in degrees is 48 ± 1° for WT; 54 ± 1° for V174A; 40 ± 1° for K159S/K163S; 50 ± 1° for K159S/K163S/V174A; 40 ± 1° for R155S/K159S/K163S; and 48 ± 1° for R155S/K159S/K163S/V174A. The radial angle in the crystallographic structure (α = 31°) is shown as a black vertical bar for reference. **(G–I)** The mean pore radius at position F171 (*r*, axial position ∼19 Å) and the number of water molecules in the hydrophobic stretch (N_{wat}, axial positions 10–25 Å). Each point represents a single snapshot of our simulation analysis. (Pearson correlation of 0.62 across all datasets.)

positive charges than STIM1-gated channels (Fig. 2, C and D). Taken together, these results support the hypothesis that the basic inner pore residues are essential for channel activation both by STIM1 and by the H134S GOF mutation.

Molecular simulations indicate that the basic pore residues promote opening of the outer hydrophobic gate

Loss of channel function in the 3S and 2S mutants could arise from many factors, including impairment in the opening of the outer channel gate, changes in ion permeation, or the closure of the pore for other unknown reasons. To address these possibilities, we performed MD simulations using the available dOrai crystal structure (PDB accession no. 4HKR) and quantified the effect of mutations of the basic charges on pore structure and hydration. We simulated the WT, V174A (corresponding to V102A in hOrai1), R155S/K159S/K163S (corresponding to the 3S hOrai1 mutant), and K159S/K163S (corresponding to the 2S hOrai1 mutant). As previously shown (Dong et al., 2013; Yamashita et al., 2017; Yeung et al., 2018; Bulla et al., 2019), simulations in WT channels revealed low but measurable levels of hydration throughout the pore, including in the hydrophobic stretch encompassing F171 and V174 (F99-V102 in hOrai1; Fig. 3 C). Moreover, the pore helices of WT and V174A dOrai displayed spontaneous counterclockwise rotations, with the average angular position of F171 shifted by 17 ± 1° and 23 ± 1°, respectively, relative to the crystallographic dOrai structure (Fig. 3 F). The pore radius of the conducting V174A channels was also wider (Fig. 3 E). These thermal fluctuations are similar to the conformations for WT and constitutively conducting Orai channels previously described by us and others (Yamashita et al., 2017; Bulla et al., 2019; Dong et al., 2019).

Analysis of the 2S and 3S mutants revealed several striking differences in pore hydration and the configuration of the pore helices compared with WT channels (Fig. 3). First, both mutants showed significant decreases in pore hydration, which was particularly prominent at two positions: (1) at the outer end of the pore around the hydrophobic gate region encompassing the F171-V174 channel gate (axial position 12–30 Å, gray-shaded area in Fig. 3 C), and (2) at the cytoplasmic end of the inner pore, at position W76. Second, the amplitude of the spontaneous (thermal) fluctuations in TM1 that evoke pore helix rotation and displacement of F171 side chains away from the pore were

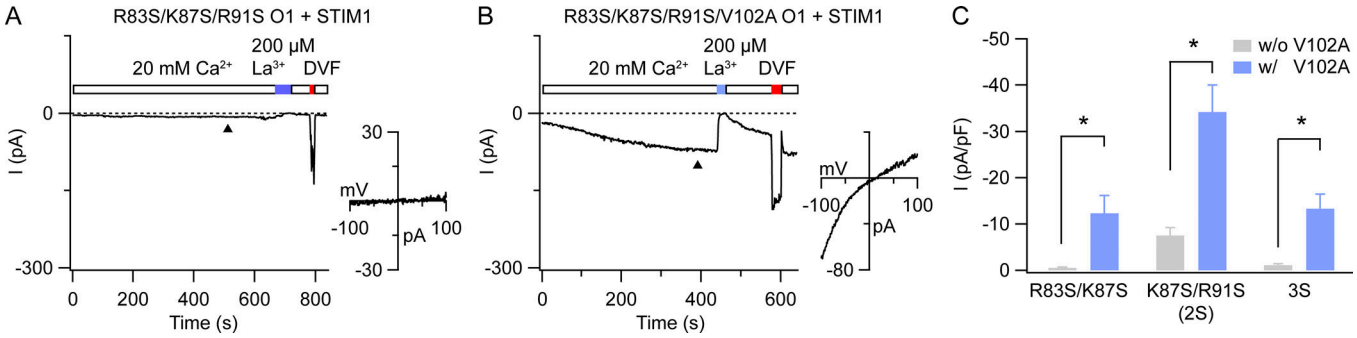

Figure 4. **The V102A mutation rescues STIM1 gating in the nonconducting inner pore serine mutants. (A and B)** The LOF phenotype of the inner pore mutant (R83S/K87S/R91S [3S]) can be rescued by adding the V102A substitution, which diminishes outer pore hydrophobicity. The insets show I–Vs obtained at the time points indicated by the arrowheads. **(C)** Summary graph of current densities (I [pA/pF]) of R83S/K87S, K87S/R91S (2S), and R83S/K87S/R91S (3S) Orai1 channels in the presence of STIM1 with and without the V102A mutation. Values are mean ± SEM (n = 6 or 7 cells per condition; *, P < 0.05, Student's t test). w/, with; w/o, without.

dramatically reduced, with an average F171 Cα rotation of only 9 ± 1° in the 3S mutant compared with 18 ± 1° in WT channels (Fig. 3 F). As a consequence, F171 residues were oriented in a pore-facing (closed) configuration to a greater extent in the 3S (and 2S) mutants compared with WT or constitutively permeant V174A channels (Fig. 3, A and F). Third, examination of the pore geometry indicated that both 3S and 2S were significantly narrower compared with WT channels, with constriction apparent in particular at the hydrophobic gate (Fig. 3 E). Note that because the Ser side chains are smaller than the endogenous Arg and Lys side chains, HOLE analysis gives the mistaken sense that the pore is dilated at the positions of these residues. However, examination of the helical positions (using center of mass of each TM1) indicates that the helical backbones are in fact more closely packed in the 2S/3S mutants (Fig. 3, G–I). Further, a plot of the TM1 pore radius against the number of water molecules in the hydrophobic stretch shows that the narrowing of the pore is correlated with loss of hydration at the hydrophobic gate (Fig. 3, G–I). We have previously observed that the extent of pore dilation in the hydrophobic gate region is correlated with the "openness" of GOF mutants (Yeung et al., 2018). Thus, the narrowing of the pore in the 2S and 3S mutants suggests that these mutants are locked into a closed configuration. And fourth, removal of the Cl^- binding sites in the inner pore (and therefore the presumptive chloride ion plug) did not appear to directly promote metrics of pore opening (pore hydration and displacement of F171 gate residues).

These results indicate that the loss of the basic inner pore residues in the 2S/3S mutants dramatically lowers the extent of hydration of the hydrophobic gate and therefore likely increases the free energy barrier for ion conduction through this region, as suggested by previous simulation studies of Orai1 (Dong et al., 2013) and of the Mg^{2+} channel, CorA (Neale et al., 2015). This change is accompanied by stabilization of F99 residues in a pore-facing configuration to close the upper gate. Thus, our simulations suggest that the presence of the basic residues promotes channel opening by favoring the wetted state of the hydrophobic gate through a long-range effect.

Loss of gating in the inner pore mutants is rescued by lowering hydrophobicity at the outer gate

Dehydration of the hydrophobic gate seen in the 3S and 2S LOF mutants suggests that the free energy barrier for gate opening becomes prohibitively high in these mutants. Can ion conduction in these mutants be rescued if pore hydration is restored by a V102A mutation? Previous studies have shown that V102A/C mutations promote pore hydration and constitutive ion permeation (McNally et al., 2012; Dong et al., 2013; Yamashita et al., 2017). Therefore, we tested whether introduction of V102A to the 3S and 2S mutations restores channel activity, analogous to the rescue of channel function seen in LOF truncation mutants of the inner pore (e.g., Δ73–85 Orai1; Li et al., 2007; Park et al., 2009; Zhou et al., 2010a; Derler et al., 2013; McNally et al., 2013; Gudlur et al., 2014).

MD simulations revealed that the addition of V174A to the 3S and 2S mutants dramatically increased pore hydration and restored the water density profile in the hydrophobic gate region close to that seen in the WT channel (Fig. 3 C). Notably, this effect was limited to the hydrophobic gate region. No change was seen in hydration at the cytoplasmic end of the pore at W76, which remained relatively dehydrated at levels similar to the 2S/3S background levels (Fig. 3 C). Furthermore, analysis of helix rotation at residue F171 and of pore radius indicated that the addition to V174A to 2S/3S also increased rotational movements of F171 away from the pore axis, with an average F171 Cα rotation angle of 18 ± 1° in the 3S/V174A mutant compared with 9 ± 1° in the 3S channel (Fig. 3 F). Quantification of the pore geometry in the hydrophobic gate region showed that V174A widened the unusually narrow pore of the 3S and 2S mutants by ∼1 Å (Fig. 3, E, H, and I). Together, these results indicate that the decrease in hydration and narrowing of the pore at the hydrophobic gate can be reversed by lowering the hydrophobicity of residue 174.

Consistent with the above predictions, electrophysiological analysis of channel activity indicated that addition of V102A to 3S and 2S mutants rescued STIM1-dependent channel activation (Fig. 4). In cells coexpressing the V102A/3S or V102A/2S mutants with STIM1, whole-cell break-in with BAPTA resulted in slow activation of large CRAC currents as seen in WT channels. Peak I_{CRAC} amplitudes at 300 s following whole-cell break-in were −13 ± 3 (pA/pF) and −34 ± 5 (pA/pF) in the V102A/3S and V102A/2S mutants, respectively (Fig. 4 C). These STIM1-gated

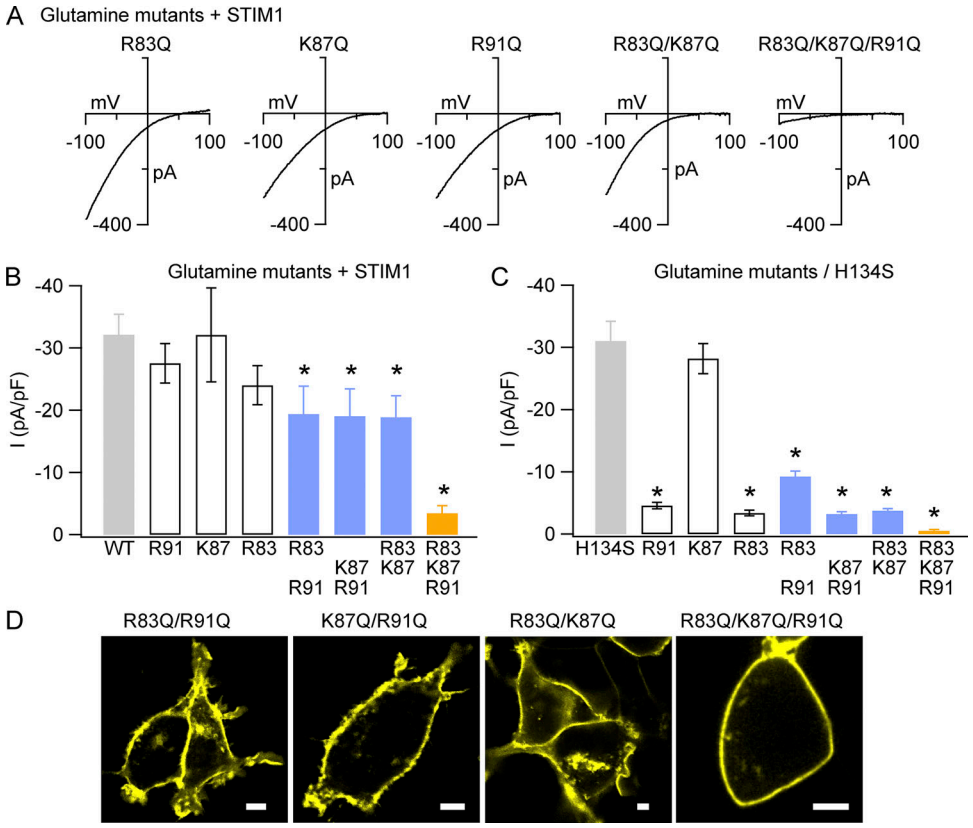

Figure 5. **The polarity of the basic domain also contributes to Orai1 channel opening. (A)** I–V relationships of Gln Orai1 mutants in 20 mM Ca^{2+} Ringer's solution. **(B and C)** Summary of the peak current amplitudes (I [pA/pF]) of WT and Gln Orai1 mutants activated by STIM1 (B), or by the GOF H134S mutant (C). Unlike the equivalent Ser mutants (Fig. 2 C), the Gln mutants are more strongly activated by STIM1, suggesting that increased polarity of Gln relative to Ser promotes Orai1 channel opening. Note that K87Q/H134S mutation had no detrimental effect on Orai1 current density. Values are mean ± SEM (n = 6–9 cells per condition; *, $P < 0.05$, Student's t test). **(D)** Expression of the indicated Q mutants in the plasma membrane. Scale bars, 5 µm.

currents were, however, not selective for Ca^{2+}, which contrasts with the high Ca^{2+} selectivity of single V102A mutant channels activated by STIM1 (McNally et al., 2012; Fig. 4 B). Interestingly, unlike the V102A single mutant, neither V102A/3S nor V102A/2S showed large constitutively active Orai1 currents. This suggests that the increase in pore hydration by V102A in these mutants is not sufficient by itself to confer significant ion conduction in the absence of an additional activating signal from STIM1. Rather, the addition of V102A restores gating by reducing the free energy separating open and closed states of the channel by favoring the wetted state of the hydrophobic gate.

Polarity of the basic region also contributes to Orai1 gating

One potential issue in the analysis of the 3S and 3A mutations is that although these amino acid side chains are uncharged, they are considerably less polar than the endogenous Arg and Lys residues, raising the possibility that the 3S and 3A mutations could elicit chemical alterations distinct from the desired electrostatic changes. To address this potential issue, we neutralized the basic residues with glutamine, an uncharged yet highly polar amino acid that is similar in size and volume to Arg and Lys. Analysis of the Gln substitutions revealed distinct differences from the properties of the Ser and Ala mutants. Specifically, unlike the single Ser substitutions of R91, K87, or R83, which showed smaller currents than WT Orai1, single Gln substitutions of these residues had essentially no effect, with current amplitudes similar to that of WT Orai1 (Fig. 5, A and B). Likewise, the R83Q/K91Q, R87Q/R91Q, and the R83Q/K87Q double (2Q) mutants all showed healthy levels of store-operated Orai1 currents (>16 pA/pF) that were significantly larger than those of the corresponding 2S mutants (compare Fig. 5, A and B, vs. Fig. 2 C). Substituting all three basic residues with Gln (producing the R83Q/K87Q/R91Q or 3Q mutant), however, largely eliminated Orai1 current (Fig. 5, A and B) without affecting trafficking of the mutant protein to the plasma membrane (Fig. 5 D). As seen for the Ser mutants, substituting the basic residues with Gln in the GOF H134S background attenuated the constitutive activation of H134S (Fig. 5 C), but again less so than the equivalent Ser substitutions (Fig. 2 D). When gated by STIM1 as well as by the H134S GOF mutant, the K87Q substitution, however, failed to halt channel activation, which is in sharp contrast to the striking reduction in current in the Ser mutant at this position (Fig. 2, C and D). Thus, although the phenotypes of the Q mutants are qualitatively similar to that of the Ser mutants, there are distinct quantitative differences in the extent of activation of the single and double Q mutants.

Taken together, these results suggest that the increased polarity of Gln relative to Ser promotes channel gating. By contrast, substituting the Arg residues at positions 83 and 91 with

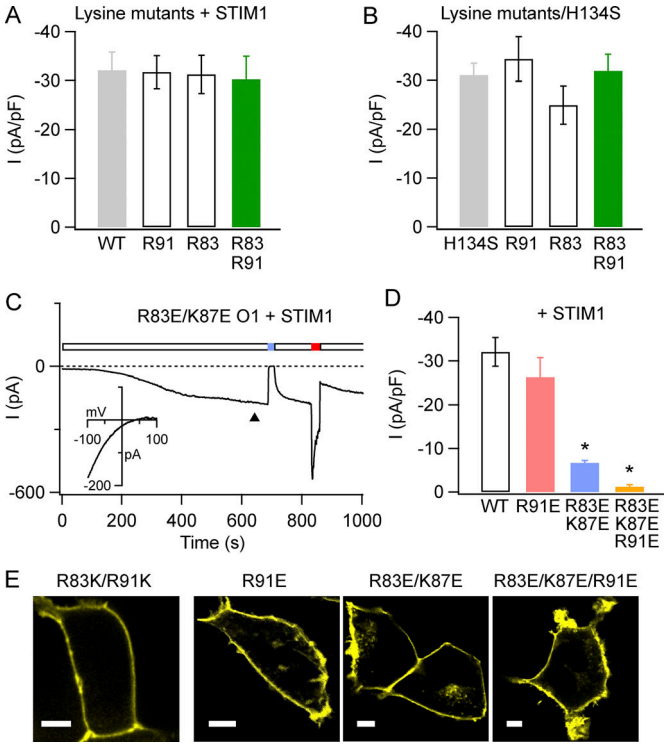

Figure 6. **Analysis of charge preserving and reversal mutations. (A and B)** Lys substitutions of R91 and R83 do not impair Orai1 activation. Summary of the peak current amplitudes (I [pA/pF]) of WT and Lys Orai1 mutants coexpressed with STIM1, or expressed alone in the presence of the GOF H134S mutant. Values are mean ± SEM (n = 6–9; *, P < 0.05, Student's t test). **(C)** By contrast, Glu substitutions resulted in progressive loss of channel function with increasing number of Glu substitutions. The trace shows a representative example from cell expressing R83E/K87E Orai1 with STIM1. **(D)** Summary of the peak current amplitudes (I [pA/pF]) of WT and Glu Orai1 mutants coexpressed with STIM1. Values are mean ± SEM (n = 6–9; *, P < 0.05, Student's t test). **(E)** Expression of the indicated K and E mutants in the plasma membrane. Scale bars, 5 µm.

equivalently charged Lys (R83K/R91K or 3K mutant) did not affect channel function. Currents in the 3K mutant were indistinguishable in amplitude from those in WT channels (Fig. 6, A and B). However, replacing the basic residues with the negatively charged glutamic acid amino acid resulted in progressive loss of channel function with an increasing number of Glu substitutions (Fig. 6, C and D). Membrane expression was not noticeably different from that of WT Orai1 channels (Fig. 6 E), indicating that differences in channel expression do not account for the loss of gating in the Glu mutants. Thus, negatively charged Glu substitutions evoke stronger inhibition of channel function than substitutions to the uncharged but equally polar Gln, likely reflecting additional consequences of the negative electrostatic potential in the former. We conclude that although a key determinant of channel function is the positive charge of the basic domain, the replacement of Arg and Lys by uncharged but strongly polar residues can also significantly boost opening of the hydrophobic gate.

W76 does not regulate pore opening

As noted above, in addition to the dehydration of the hydrophobic gate, molecular simulations show a significant loss of hydration at the cytoplasmic end of the pore at residue W76 in the 2S/3S mutants. This is interesting as W76 has previously been implicated as a potential gate in a different mode of Orai1 gating involving calcium-dependent inactivation (Mullins and Lewis, 2016). Specifically, mutations that remove the bulky hydrophobic side chain of W76 abrogate inactivation (Mullins and Lewis, 2016). To test whether the side-chain and hydrophobicity of W76 also regulate channel activation in response to STIM1, we tested the W76A and W76S mutations, which should increase hydrophilicity at this pore locus while considerably shortening the side chain. In marked contrast to the restoration of channel function by V102A, the addition of W76A/S to the 3S mutant did not restore channel function in STIM1-coexpressing cells (Fig. S3, B–D). Molecular simulations indicate that the W76A mutation (W148A in dOrai) did not appreciably alter the hydration at the outer hydrophobic gate or alter the pore radius at this location even though hydration and pore radius were increased locally around residue 76 (Fig. S3, G and I). In addition, unlike mutations of V102 or F99, the single mutants (W76A/S) were not constitutively active in the absence of STIM1. These observations indicate that although the removal of the basic residues diminishes hydration at both ends of the pore, only the hydration of the outer hydrophobic gate is functionally linked to channel opening. We conclude that the LOF phenotype of the 3S mutation is caused by an increase in the hydrophobic barrier in the outer pore and not by blockade of ion conduction by W76 at the cytoplasmic end of the pore.

The human mutation R91W dehydrates the pore and stabilizes closure of the hydrophobic gate

Within the cluster of basic residues of the inner pore, the role of R91 is of particular importance because a human mutation, R91W, abolishes Orai1 channel function, leading to a devastating immunodeficiency and death (Feske et al., 2005; Feske et al., 2006). Previous studies have suggested that introduction of the bulky Trp at this position interferes with ion conduction due to steric occlusion of the inner pore (Derler et al., 2009; McNally et al., 2009; Zhang et al., 2011). However, our observations indicating that inner pore basic residues evoke long-range effects on the configuration of the channel gate raise the possibility that in addition to these steric effects, pore closure may also be mediated by dehydration of the outer hydrophobic gate. To address this hypothesis, we performed MD simulations of the K163W mutant (corresponding to R91 in hOrai1; Fig. 7). This analysis revealed that K163W evokes several significant alterations in the pore that effectively stabilize the closed channel state. In particular, K163W showed a much lower extent of pore helix rotation compared with WT (Fig. 7 F). This decrease in rotation/twisting was accompanied by significant narrowing (~1.5 Å) of the pore radius at the F171 channel gate (Fig. 7, E and G) and substantial decrease in pore hydration, especially in the hydrophobic region (Fig. 7, C and G). These results indicate that K163W produces significant de-wetting of the pore, especially in and around the hydrophobic gate, and locks the channel in the closed state. Further, adding the V174A mutation to K163W significantly restored pore hydration at the hydrophobic gate (Fig. 7 C) and the amplitude of the counterclockwise fluctuations of the

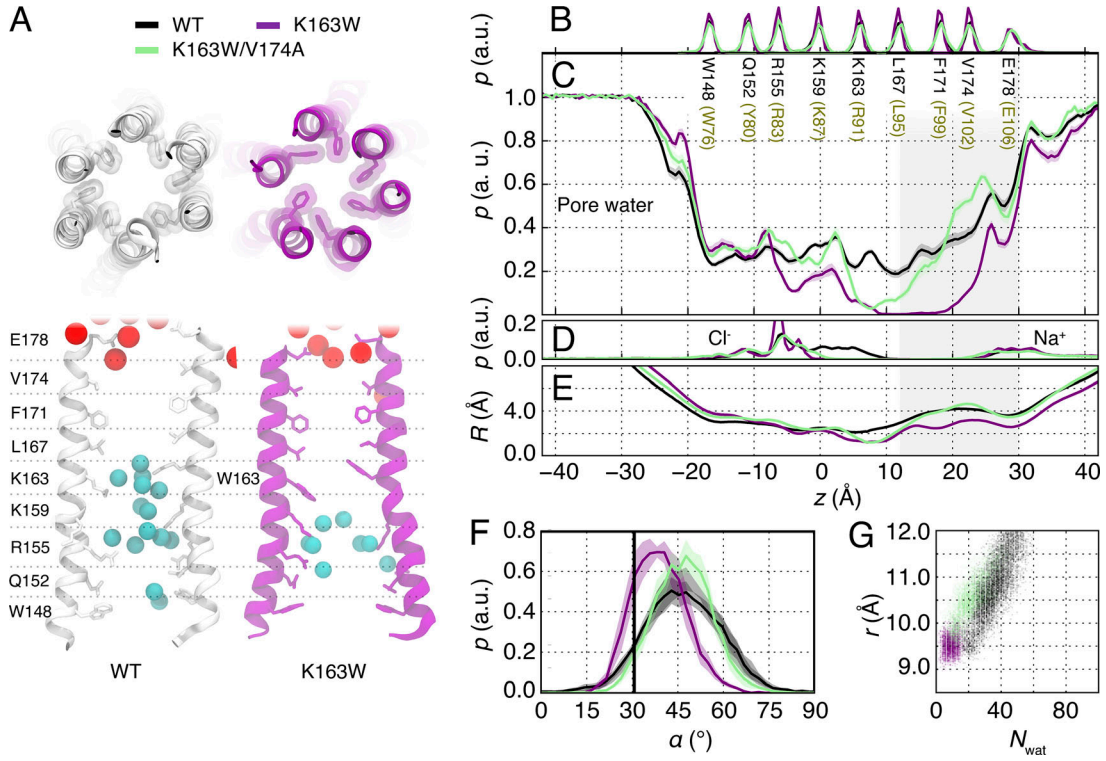

Figure 7. **K163W (R91W in hOrai1) decreases pore hydration and stabilizes closure of the hydrophobic gate. (A)** Top: Molecular renderings of snapshots from MD simulations of WT (gray) and K163W (purple) as viewed from the top. Bottom: Pairs of diagonal subunits viewed from the side. Na^+ and Cl^- are depicted as red and cyan spheres, respectively. **(B)** Probability distributions of Cα atoms for pore-lining residues along the pore axis (z), averaged over all subunits for all simulation repeats. **(C)** Relative probability distribution of water oxygen atoms. **(D)** Na^+, and Cl^- ions along the pore axis (z), normalized with respect to bulk water. **(E)** Average pore radius computed using HOLE (*R*). **(F)** Probability distribution of the radial angle of residue 171 (α), defined as the angle between the pore axis, the center of mass of the two helical turns centered at residue 171, and the Cα atom of residue 171. The mean and standard error of mean of these distributions across all simulation repeats in degrees is 48 ± 1° for WT, 38 ± 2° for K163W, and 42 ± 1° for K163W/V174A. **(G)** The mean pore radius at position F171 (*r*, axial position ∼19 Å) and the number of water molecules in the hydrophobic stretch (N_{wat}, axial positions 10–25 Å).

pore helix (Fig. 7 F) to levels comparable to WT dOrai channels. Thus, these simulations predicted that introduction of V102A to R91W should rescue channel activity. Accordingly, electrophysiological analysis indicated that disrupting the hydrophobic gate with the V102A mutation markedly restored activation of R91W Orai1 by STIM1 (Fig. 8). R91W/V102A-expressing cells showed relatively large currents of 16 ± 3 pA/pF compared with 0.3 ± 0.1 pA/pF in the single R91W mutant. Interestingly, in contrast to WT Orai1 channels or the single V102A mutant channels, these R91W/V102A currents were nonselective with a V_{rev} of ∼0 mV (Fig. 8 A). This feature is similar to the loss of Ca^{2+} selectivity in the STIM1-activated 2S/3S mutants (Fig. 4 B) and indicates that R91W blocks a STIM1-mediated conformational change at the selectivity filter (E106) that confers high Ca^{2+} selectivity. We conclude that the R91W mutation dewets the pore at the hydrophobic gate and that this effect contributes to the LOF phenotype and immunodeficiency associated with this human mutation.

Discussion

Ever since the discovery that the inner pore of the Orai channels harbors a hub of positive charges in the ion conduction pathway, the role of these charges has been the topic of much debate. It has been widely postulated that these positive charges present an electrostatic energy barrier for cation conduction and function as a channel gate to regulate the closed–open transition. However, here we show that the positive charges are essential for ion conduction through the pore and likely play an entirely different role by promoting hydration/wetting of the hydrophobic gate to stabilize channel opening. These findings modify the prevailing views on Orai1 gating and reveal an intriguing molecular design of Orai1 that facilitates channel activation.

The notion that the basic residues may form an inner pore gate came from early observations indicating that R91 residues are in close enough proximity that Cys substitutions of these residues can be cross-linked by diamide to block ion conduction (Zhang et al., 2011). These observations were further supported by the finding that cross-linking of R91C is reduced in the presence of STIM1. However, it is worth noting that intersubunit cross-linking of R91C is not unique to R91 but is also seen at many other non–gate-forming pore residues, including E106, L95, and in the outer pore at D110, D112, and Q108 (McNally et al., 2009; Zhou et al., 2010b). Moreover, blockade of ion conduction by the R91W substitution, which was also interpreted in support of a gating role for R91, is not unique to the position but seen at all pore-lining TM1 residues (Fig. 1 D). In a variation of the above model, another study suggested that the

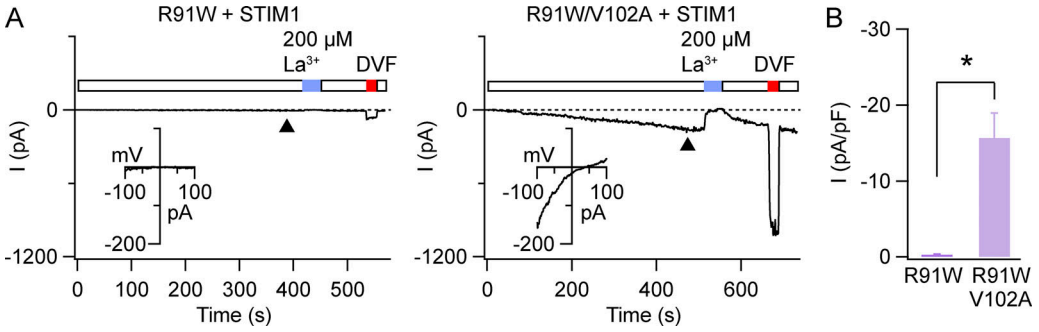

Figure 8. **Addition of V102A to the R91W rescues channel activation by STIM1 in this mutant. (A and B)** Example traces and mean current densities of Orai1 currents (R91W or R91W/V102A Orai1) in the presence of STIM1. The insets show I–Vs obtained at the time points indicated by the arrowheads. Values are mean ± SEM (n = 6; *, P < 0.05, Student's t test).

basic residues may contribute to blocking of ion conduction in the closed state by coordinating an anion plug (Hou et al., 2012). Both models predict that structural rearrangement of the inner pore gate (or loss of the anion plug) should destabilize the closed channel state to promote channel opening. However, as first reported by Hou et al. (2018), we find that mutations at R91 and the other basic residues do not elicit spontaneous pore opening (Fig. 1 B). These findings indicate that removal of the basic residues in the inner pore and ensuing release of Cl^- ions do not destabilize the resting, closed state of Orai1.

On the contrary, neutralizing the basic residues eliminates pore opening in a charge-dependent manner (Figs. 2, 5, and 6), indicating that the positively charged residues are essential for ionic conduction. We find that the basic residues contribute to pore hydration, especially in and around the hydrophobic stretch (Figs. 3 and 7), and as such, promote the opening of the hydrophobic gate. Several lines of evidence support this analysis. First, MD simulations show that loss of the basic residues (even just two of the three charges per protomer) dramatically dehydrates the upper pore, especially around the hydrophobic gate region (Fig. 3 C). Second, in the 3S/2S mutants, dewetting of the upper pore is accompanied by reorientation of the F99 residues such that they are stabilized in close proximity to each other in a closed pore configuration (Fig. 3, A and F). Third, the V102A mutation rescues both pore hydration and channel function in the 3S/2S mutants (Figs. 3 and 4) as well as in the immunodeficiency-associated R91W mutation (Figs. 7 and 8), indicating that the dewetting imposed by the loss of the basic residues can be reversed by lowering pore hydrophobicity. The conspicuous rescue of channel function and pore hydration by the V102A mutation reaffirms the critical importance of the hydrophobic gate for channel opening.

A recent simulation study of the human Orai1 channel reported striking enhancement of interactions between R91 and S90 of neighboring subunits in GOF H134A mutant channels, which led the authors to conclude that opening of an R91 gate is mediated by twisting of the side chain via hydrogen bond interactions with S90 (Frischauf et al., 2017). However, in our simulations of the dOrai channels, we did not observe interactions between K163 (hOrai1 R91) and S162 (hOrai1 S90) of the neighboring subunit, nor did we see K163 adopting different conformations in the activating H206S/C (hOrai1 H134S/C) variants. Specifically, in our analysis of the previously described, constitutively active H206S mutant, K163-S162 hydrogen bonds were seen in <1% of the frames, a value that we believe is too low to mediate a role in pore opening. Somewhat surprisingly, Frischauf et al. (2017) also did not observe the spontaneous thermal pore helix rotations/twisting motions at F99 in their MD simulations, in contrast to our studies (Yamashita et al., 2017; Yeung et al., 2018). These differences may result from divergent computational modeling methodologies, including the choice of force field, homology modeling of the human Orai1 channel, presence of counterions and excess salt (not reported in Frischauf et al., 2017), introduction of bound cholesterol molecules in Frischauf et al. (2017), and extent of sampling. However, the lack of noticeable K163-S162 interactions in our simulations is consistent with experimental findings indicating that mutations of R91 or S90 that would be expected to disrupt a putative S90-R91 interaction do not impede STIM1-mediated channel gating (Fig. 1 E). We note that two other simulation studies have also reported discrete rotations of the pore helix at F99 with concomitant increase in pore hydration in the constitutively open H134C/A and, to a lower extent, in WT Orai1 channels (Bulla et al., 2019; Dong et al., 2019). Moreover, the finding that F99 is displaced away from the pore is supported by the differential accessibility of thiol reagents to F99C in STIM1-bound and STIM1-free Orai1 channels (Yamashita et al., 2017). Thus, more studies are needed to address the origin and significance of the differences between the various simulation studies.

Two recent publications have reported structures of the "open" gain-of-function dOrai H206A and P288L mutants (Hou et al., 2018; Liu et al., 2019). Both structures showed very large (>10 Å) dilations of the inner pore helices (relative to the presumably closed dOrai structure, PDB accession no. 4HKR), which was interpreted in terms of release of a putative anion plug that blocks ion conduction in the closed channels. However, this interpretation is not consistent with observations that the functional activity of Orai1 channels is inversely correlated with the presence of inner pore Cl^- ions, with mutations that reduce Cl^- occupancy decreasing channel activation (Figs. 2, 5, and 6). Further, at the low resolution of these structures, neither shifts

in the position of amino acids side chains nor modest alterations in the main chain (such as small helical rotations) could be discerned. Thus, the precise roles of inner pore dilation and the conformational changes in the upper pore underlying pore opening await higher-resolution Orai structures.

Although the precise physio-chemical factors by which the basic residues promote pore hydration need to be determined, we speculate that this mechanism may be rationalized in terms of the Hofmeister effect, wherein salts regulate hydration of protein surfaces (Kunz et al., 2004; Jungwirth and Cremer, 2014). Our data show that loss of basic residues eliminates anion occupancy of the inner pore as well as gating (Figs. 2 and 3). Thus, pore hydration and pore opening may be regulated by changes in the local ionic strength, and more specifically, by the anion concentration in the inner pore. We favor the possibility that modulation of pore hydration results from a "salting-in" effect, in which salts at low to moderate doses increase protein solubility by reducing hydrophobic interactions between protein surfaces (Kunz et al., 2004; Jungwirth and Cremer, 2014; Okur et al., 2017). Thus, in this scenario, removal of the basic residues would minimize the local ionic strength to dehydrate protein surfaces, resulting in greater aggregation of hydrophobic pore surfaces and pore closure.

Regardless of the precise mechanism, from a functional standpoint, the finding that the inner pore basic residues promote pore opening by increasing hydration at the channel gate may have important implications for CRAC channel gating. Past work has shown that the CRAC channel activation process is exquisitely cooperative, resulting in the recruitment of silent channels into a high open probability (P_o) state (P_o ~0.7) following store depletion or during potentiation induced by the small molecule 2-amino diphenylborate (Prakriya and Lewis, 2006; Kilch et al., 2013; Yamashita and Prakriya, 2014; Mullins et al., 2016; Yen and Lewis, 2018). The molecular basis of how the channel is stabilized in the high P_o state is largely unknown. Hydration of the pore by the inner pore basic residues could represent a key physical mechanism for opening and maintaining the pore in a high P_o state. Given that CRAC channels have an extremely low unitary conductance (<1 pS), this role of the inner pore residues in promoting pore opening may be critical for maintaining Ca^{2+} influx at sufficient levels needed to effectively drive cellular functions. The devastating immunodeficiency resulting from the loss of Orai1 gating in the R91W mutation highlights the importance of this gating role for human health.

Acknowledgments

Merritt C. Maduke served as editor.

We thank members of the laboratory for helpful discussions.

Molecular simulations conducted in this work were enabled by supercomputing resources and support provided by SciNet and Compute Canada (www.computecanada.ca). This work was supported by National Institutes of Health grants NS057499 and GM114210 (to M. Prakriya), Canadian Institutes of Health Research grant MOP130461 (to R. Pomès), and National Institutes of Health Predoctoral Fellowship F31NS101830 (to P.S.-W. Yeung). Northwestern University's Center for Advanced Microscopy is supported by National Institutes of Health grant NCRR 1S10 RR031680.

The authors declare no competing financial interests.

Author contributions: M. Yamashita performed and analyzed all the electrophysiological experiments and confocal imaging with help from P.S.-W. Yeung and M.M. Maneshi. C.E. Ing and R. Pomès designed and performed the molecular dynamics simulations; M. Yamashita and C.E. Ing prepared the figures; all authors designed the experiments, analyzed the results, and wrote and edited the manuscript.

Submitted: 13 May 2019
Revised: 25 September 2019
Accepted: 5 November 2019

References

Abraham, M.J.. 2015. GROMACS: High performance molecular simulations through multi-level parallelism from laptops to supercomputers. *SoftwareX*. 1–2:19–25.

Best, R.B., X. Zhu, J. Shim, P.E. Lopes, J. Mittal, M. Feig, and A.D. Mackerell Jr. 2012. Optimization of the additive CHARMM all-atom protein force field targeting improved sampling of the backbone φ, ψ and side-chain χ(1) and χ(2) dihedral angles. *J. Chem. Theory Comput.* 8:3257–3273. https://doi.org/10.1021/ct300400x

Bulla, M., G. Gyimesi, J.H. Kim, R. Bhardwaj, M.A. Hediger, M. Frieden, and N. Demaurex. 2019. ORAI1 channel gating and selectivity is differentially altered by natural mutations in the first or third transmembrane domain. *J. Physiol.* 597:561–582. https://doi.org/10.1113/JP277079

Darden, T., D. York, and L. Pedersen. 1993. Particle Mesh Ewald - an N.Log(N) Method for Ewald Sums in Large Systems. *J. Chem. Phys.* 98: 10089–10092. https://doi.org/10.1063/1.464397

Derler, I., M. Fahrner, O. Carugo, M. Muik, J. Bergsmann, R. Schindl, I. Frischauf, S. Eshaghi, and C. Romanin. 2009. Increased hydrophobicity at the N-terminus/membrane interface impairs gating of the SCID-related ORAI1 mutant. *J. Biol. Chem.* https://doi.org/10.1074/jbc.M808312200

Derler, I., P. Plenk, M. Fahrner, M. Muik, I. Jardin, R. Schindl, H.J. Gruber, K. Groschner, and C. Romanin. 2013. The extended transmembrane Orai1 N-terminal (ETON) region combines binding interface and gate for Orai1 activation by STIM1. *J. Biol. Chem.* 288:29025–29034. https://doi.org/10.1074/jbc.M113.501510

Dong, H., G. Fiorin, V. Carnevale, W. Treptow, and M.L. Klein. 2013. Pore waters regulate ion permeation in a calcium release-activated calcium channel. *Proc. Natl. Acad. Sci. USA.* 110:17332–17337. https://doi.org/10.1073/pnas.1316969110

Dong, H., M.L. Klein, and G. Fiorin. 2014. Counterion-assisted cation transport in a biological calcium channel. *J. Phys. Chem. B.* 118:9668–9676. https://doi.org/10.1021/jp5059897

Dong, H., Y. Zhang, R. Song, J. Xu, Y. Yuan, J. Liu, J. Li, S. Zheng, T. Liu, B. Lu, et al. 2019. Toward a Model for Activation of Orai Channel. iScience. 16: 356–367. https://doi.org/10.1016/j.isci.2019.05.041

Essmann, U., L. Perera, M.L. Berkowitz, T. Darden, H. Lee, and L.G. Pedersen. 1995. A Smooth Particle Mesh Ewald Method. *J. Chem. Phys.* 103: 8577–8593. https://doi.org/10.1063/1.470117

Feske, S. 2009. ORAI1 and STIM1 deficiency in human and mice: roles of store-operated Ca^{2+} entry in the immune system and beyond. *Immunol. Rev.* 231:189–209. https://doi.org/10.1111/j.1600-065X.2009.00818.x

Feske, S. 2010. CRAC channelopathies. *Pflugers Arch.* 460:417–435. https://doi.org/10.1007/s00424-009-0777-5

Feske, S., M. Prakriya, A. Rao, and R.S. Lewis. 2005. A severe defect in CRAC Ca^{2+} channel activation and altered K^+ channel gating in T cells from immunodeficient patients. *J. Exp. Med.* 202:651–662. https://doi.org/10.1084/jem.20050687

Feske, S., Y. Gwack, M. Prakriya, S. Srikanth, S.H. Puppel, B. Tanasa, P.G. Hogan, R.S. Lewis, M. Daly, and A. Rao. 2006. A mutation in Orai1 causes immune deficiency by abrogating CRAC channel function. *Nature.* 441:179–185. https://doi.org/10.1038/nature04702

Fiser, A., and A. Sali. 2003. Modeller: generation and refinement of homology-based protein structure models. *Methods Enzymol.* 374: 461–491. https://doi.org/10.1016/S0076-6879(03)74020-8

Frischauf, I., M. Litviňuková, R. Schober, V. Zayats, B. Svobodová, D. Bonhenry, V. Lunz, S. Cappello, L. Tociu, D. Reha, et al. 2017. Transmembrane helix connectivity in Orai1 controls two gates for calcium-dependent transcription. *Sci. Signal.* 10:eaao0358. https://doi.org/10.1126/scisignal.aao0358

Gudlur, A., A. Quintana, Y. Zhou, N. Hirve, S. Mahapatra, and P.G. Hogan. 2014. STIM1 triggers a gating rearrangement at the extracellular mouth of the ORAI1 channel. *Nat. Commun.* 5:5164. https://doi.org/10.1038/ncomms6164

Hess, B. 2008. P-LINCS: A parallel linear constraint solver for molecular simulation. *J. Chem. Theory Comput.* 4:116–122. https://doi.org/10.1021/ct700200b

Hoover, W.G. 1985. Canonical dynamics: Equilibrium phase-space distributions. *Phys. Rev. A Gen. Phys.* 31:1695–1697. https://doi.org/10.1103/PhysRevA.31.1695

Hou, X., L. Pedi, M.M. Diver, and S.B. Long. 2012. Crystal structure of the calcium release-activated calcium channel Orai. *Science.* 338:1308–1313. https://doi.org/10.1126/science.1228757

Hou, X., S.R. Burstein, and S.B. Long. 2018. Structures reveal opening of the store-operated calcium channel Orai. *eLife.* 7:e36758. https://doi.org/10.7554/eLife.36758

Jo, S., T. Kim, and W. Im. 2007. Automated builder and database of protein/membrane complexes for molecular dynamics simulations. *PLoS One.* 2: e880. https://doi.org/10.1371/journal.pone.0000880

Jorgensen, W.L., J. Chandrasekhar, J.D. Madura, R.W. Impey, and M.L. Klein. 1983. Comparison of Simple Potential Functions for Simulating Liquid Water. *J. Chem. Phys.* 79:926–935. https://doi.org/10.1063/1.445869

Jungwirth, P., and P.S. Cremer. 2014. Beyond Hofmeister. *Nat. Chem.* 6: 261–263. https://doi.org/10.1038/nchem.1899

Kilch, T., D. Alansary, M. Peglow, K. Dörr, G. Rychkov, H. Rieger, C. Peinelt, and B.A. Niemeyer. 2013. Mutations of the Ca2+-sensing stromal interaction molecule STIM1 regulate Ca2+ influx by altered oligomerization of STIM1 and by destabilization of the Ca2+ channel Orai1. *J. Biol. Chem.* 288:1653–1664. https://doi.org/10.1074/jbc.M112.417246

Klauda, J.B., R.M. Venable, J.A. Freites, J.W. O'Connor, D.J. Tobias, C. Mondragon-Ramirez, I. Vorobyov, A.D. MacKerell Jr., and R.W. Pastor. 2010. Update of the CHARMM all-atom additive force field for lipids: validation on six lipid types. *J. Phys. Chem. B.* 114:7830–7843. https://doi.org/10.1021/jp101759q

Kunz, W., J. Henle, and B.W. Ninham. 2004. 'Zur Lehre von der Wirkung der Salze' (about the science of the effect of salts): Franz Hofmeister's historical papers. *Curr Opin Colloid In.* 9:19–37. https://doi.org/10.1016/j.cocis.2004.05.005

Lacruz, R.S., and S. Feske. 2015. Diseases caused by mutations in ORAI1 and STIM1. *Ann. N. Y. Acad. Sci.* 1356:45–79. https://doi.org/10.1111/nyas.12938

Li, Z., J. Lu, P. Xu, X. Xie, L. Chen, and T. Xu. 2007. Mapping the interacting domains of STIM1 and Orai1 in Ca^{2+} release-activated Ca^{2+} channel activation. *J. Biol. Chem.* 282:29448–29456. https://doi.org/10.1074/jbc.M703573200

Liu, X., G. Wu, Y. Yu, X. Chen, R. Ji, J. Lu, X. Li, X. Zhang, X. Yang, and Y. Shen. 2019. Molecular understanding of calcium permeation through the open Orai channel. *PLoS Biol.* 17:e3000096. https://doi.org/10.1371/journal.pbio.3000096

MacKerell, A.D., D. Bashford, M. Bellott, R.L. Dunbrack, J.D. Evanseck, M.J. Field, S. Fischer, J. Gao, H. Guo, S. Ha, et al. 1998. All-atom empirical potential for molecular modeling and dynamics studies of proteins. *J. Phys. Chem. B.* 102:3586–3616. https://doi.org/10.1021/jp973084f

McNally, B.A., M. Yamashita, A. Engh, and M. Prakriya. 2009. Structural determinants of ion permeation in CRAC channels. *Proc. Natl. Acad. Sci. USA.* 106:22516–22521. https://doi.org/10.1073/pnas.0909574106

McNally, B.A., A. Somasundaram, M. Yamashita, and M. Prakriya. 2012. Gated regulation of CRAC channel ion selectivity by STIM1. *Nature.* 482: 241–245. https://doi.org/10.1038/nature10752

McNally, B.A., A. Somasundaram, A. Jairaman, M. Yamashita, and M. Prakriya. 2013. The C- and N-terminal STIM1 binding sites on Orai1 are required for both trapping and gating CRAC channels. *J. Physiol.* 591: 2833–2850. https://doi.org/10.1113/jphysiol.2012.250456

Mullins, F.M., and R.S. Lewis. 2016. The inactivation domain of STIM1 is functionally coupled with the Orai1 pore to enable Ca2+-dependent inactivation. *J. Gen. Physiol.* 147:153–164. https://doi.org/10.1085/jgp.201511438

Mullins, F.M., M. Yen, and R.S. Lewis. 2016. Orai1 pore residues control CRAC channel inactivation independently of calmodulin. *J. Gen. Physiol.* 147: 137–152. https://doi.org/10.1085/jgp.201511437

Neale, C., N. Chakrabarti, P. Pomorski, E.F. Pai, and R. Pomès. 2015. Hydrophobic Gating of Ion Permeation in Magnesium Channel CorA. *PLOS Comput. Biol.* 11:e1004303. https://doi.org/10.1371/journal.pcbi.1004303

Nose, S. 1984. A Molecular-Dynamics Method for Simulations in the Canonical Ensemble. *Mol. Phys.* 52:255–268. https://doi.org/10.1080/00268978400101201

Nose, S., and M.L. Klein. 1983. Constant Pressure Molecular-Dynamics for Molecular-Systems. *Mol. Phys.* 50:1055–1076. https://doi.org/10.1080/00268978300102851

Okur, H.I., J. Hladílková, K.B. Rembert, Y. Cho, J. Heyda, J. Dzubiella, P.S. Cremer, and P. Jungwirth. 2017. Beyond the Hofmeister Series: Ion-Specific Effects on Proteins and Their Biological Functions. *J. Phys. Chem. B.* 121:1997–2014. https://doi.org/10.1021/acs.jpcb.6b10797

Pall, S., and B. Hess. 2013. A flexible algorithm for calculating pair interactions on SIMD architectures. *Comput. Phys. Commun.* 184:2641–2650. https://doi.org/10.1016/j.cpc.2013.06.003

Park, C.Y., P.J. Hoover, F.M. Mullins, P. Bachhawat, E.D. Covington, S. Raunser, T. Walz, K.C. Garcia, R.E. Dolmetsch, and R.S. Lewis. 2009. STIM1 clusters and activates CRAC channels via direct binding of a cytosolic domain to Orai1. *Cell.* 136:876–890. https://doi.org/10.1016/j.cell.2009.02.014

Parrinello, M., and A. Rahman. 1980. Crystal-Structure and Pair Potentials - a Molecular-Dynamics Study. *Phys. Rev. Lett.* 45:1196–1199. https://doi.org/10.1103/PhysRevLett.45.1196

Prakriya, M., and R.S. Lewis. 2006. Regulation of CRAC channel activity by recruitment of silent channels to a high open-probability gating mode. *J. Gen. Physiol.* 128:373–386. https://doi.org/10.1085/jgp.200609588

Prakriya, M., and R.S. Lewis. 2015. Store-Operated Calcium Channels. *Physiol. Rev.* 95:1383–1436. https://doi.org/10.1152/physrev.00020.2014

Smart, O.S., J.G. Neduvelil, X. Wang, B.A. Wallace, and M.S. Sansom. 1996. HOLE: a program for the analysis of the pore dimensions of ion channel structural models. *J. Mol. Graph.* 14:354–360: 376. https://doi.org/10.1016/S0263-7855(97)00009-X

Verlet, L.. 1967. Computer Experiments on Classical Fluids. I. Thermodynamical Properties of Lennard-Jones Molecules. *Phys. Rev.* 159:98–103.

Yamashita, M., and M. Prakriya. 2014. Divergence of $Ca^{(2+)}$ selectivity and equilibrium $Ca^{(2+)}$ blockade in a $Ca^{(2+)}$ release-activated $Ca^{(2+)}$ channel. *J. Gen. Physiol.* 143:325–343. https://doi.org/10.1085/jgp.201311108

Yamashita, M., P.S. Yeung, C.E. Ing, B.A. McNally, R. Pomès, and M. Prakriya. 2017. STIM1 activates CRAC channels through rotation of the pore helix to open a hydrophobic gate. *Nat. Commun.* 8:14512. https://doi.org/10.1038/ncomms14512

Yen, M., and R.S. Lewis. 2018. Physiological CRAC channel activation and pore properties require STIM1 binding to all six Orai1 subunits. *J. Gen. Physiol.* 150:1373–1385. https://doi.org/10.1085/jgp.201711985

Yeung, P.S., M. Yamashita, C.E. Ing, R. Pomès, D.M. Freymann, and M. Prakriya. 2018. Mapping the functional anatomy of Orai1 transmembrane domains for CRAC channel gating. *Proc. Natl. Acad. Sci. USA.* 115: E5193–E5202. https://doi.org/10.1073/pnas.1718373115

Zhang, S.L., A.V. Yeromin, J. Hu, A. Amcheslavsky, H. Zheng, and M.D. Cahalan. 2011. Mutations in Orai1 transmembrane segment 1 cause STIM1-independent activation of Orai1 channels at glycine 98 and channel closure at arginine 91. *Proc. Natl. Acad. Sci. USA.* 108:17838–17843. https://doi.org/10.1073/pnas.1114821108

Zhou, Y., P. Meraner, H.T. Kwon, D. Machnes, M. Oh-hora, J. Zimmer, Y. Huang, A. Stura, A. Rao, and P.G. Hogan. 2010a. STIM1 gates the store-operated calcium channel ORAI1 in vitro. *Nat. Struct. Mol. Biol.* 17: 112–116. https://doi.org/10.1038/nsmb.1724

Zhou, Y., S. Ramachandran, M. Oh-Hora, A. Rao, and P.G. Hogan. 2010b. Pore architecture of the ORAI1 store-operated calcium channel. *Proc. Natl. Acad. Sci. USA.* 107:4896–4901. https://doi.org/10.1073/pnas.1001169107

Supplemental material

Yamashita et al., https://doi.org/10.1085/jgp.201912397

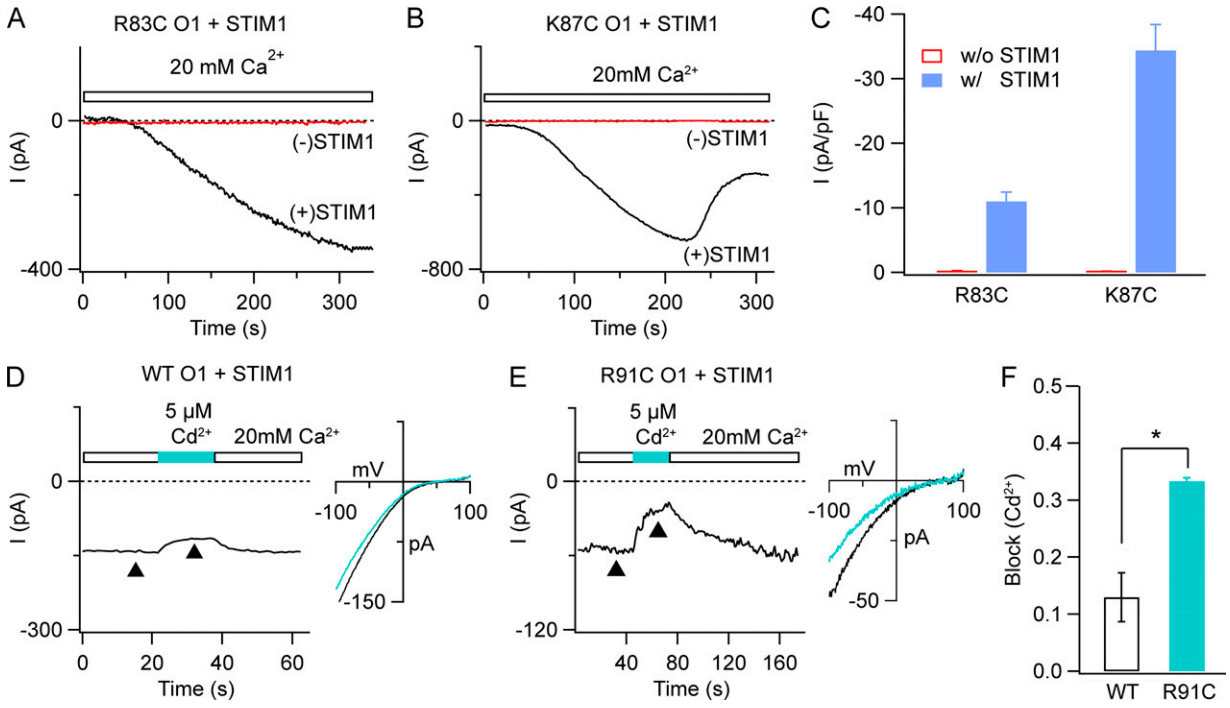

Figure S1. **Functional analysis of inner pore Cys mutants. (A and B)** The R83C and K87C mutant channels are closed in the absence of STIM1, but readily activated by STIM1. **(C)** Summary of the peak current amplitudes of R83C and K87C Orai1 mutants in the absence and presence of STIM1 in HEK293 cells. Values are mean ± SEM (n = 6). **(D and E)** Blockade of I_{CRAC} in STIM1-gated WT and R91C Orai1 channels by 5 μM Cd^{2+}. Arrowheads indicate time points where current amplitudes were measures before and after Cd^{2+} application. **(F)** Summary of Cd^{2+} inhibition of WT (n = 8) and R91C (n = 6) Orai1 channels. Values are mean ± SEM (*, P < 0.05; Student's t test).

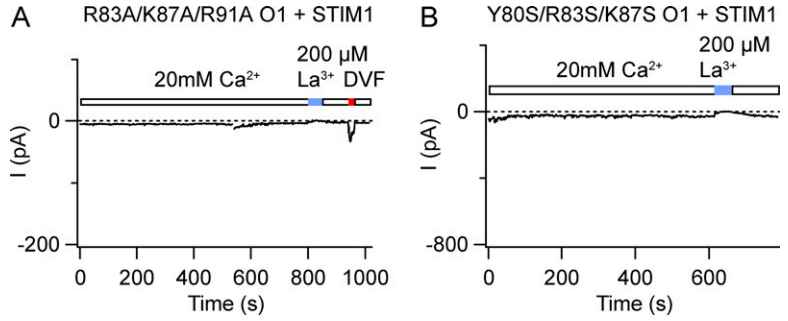

Figure S2. **The LOF phenotype of the inner pore mutant. (A and B)** Neutralizing the inner pore basic residues R83, K87, and R91 to Ala (R83A/K87A/R91A) results in nonfunctional Orai1 channels. Likewise, mutation of the inner pore residues Y80, R83, and K87 to Ser (Y80S/R83S/K87S) abrogates STIM1-mediated channel activation (n = 6 cells per condition).

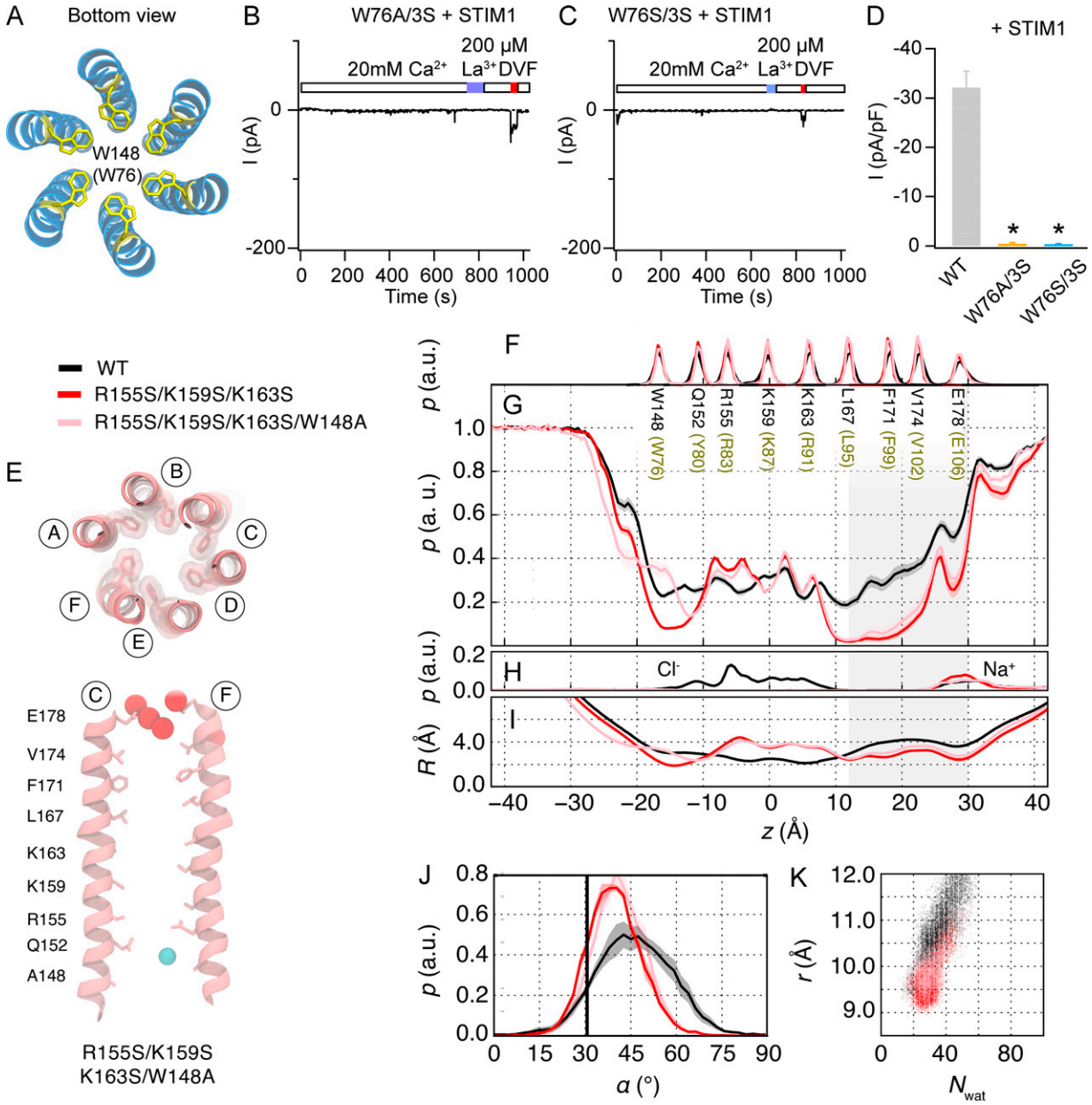

Figure S3. **W76 does not contribute to the loss of Orai1 gating in the 2S/3S mutants. (A)** A cartoon showing a bottom view of the positions of W148 (W76 in hOrai1) in the dOrai crystal structure. **(B and C)** Removing the hydrophobic barrier at W76 by mutating this residue to Ala (W76A) or Ser (W76S) does not rescue the LOF phenotype of the R83S/K87S/R91S(3S) mutant. **(D)** Summary of the peak current amplitudes of WT and W76 Orai1 mutants channels in the presence of STIM1. Values are mean ± SEM (n = 6; *, P < 0.05, Student's t test). **(E)** Top: Molecular rendering of a snapshot from MD simulations of R155S/K159S/K163S/W148A as viewed from the top. Bottom: Pairs of diagonal subunits viewed from the side. Na^+ and Cl^- are depicted as red and cyan spheres, respectively. **(F)** Probability distributions of protein Cα atoms for pore-lining residues along the pore axis (z), averaged over all subunits for all simulation repeats. **(G and H)** Relative probability distribution of water oxygen atoms, Na^+ (H), and Cl^- ions along the pore axis (z), normalized with respect to bulk water. **(I)** Average pore radius computed using HOLE (R). **(J)** Probability distribution of the radial angle of residue 171 (α), defined as the angle between the pore axis, the center of mass of the two helical turns centered at residue 171, and the Cα atom of residue 171. The mean and standard error of mean of these distributions across all simulation repeats in degrees is 48 ± 1° for WT, 40 ± 1° for R155S/K159S/K163S, and 42 ± 1° for R155S/K159S/K163S/W148A. **(K)** The mean pore radius at position F171 (r, axial position ~19 Å) and the number of water molecules in the hydrophobic stretch (N_{wat}, axial positions 10–25 Å).